





Article

Structural, Electronic, and Optical Properties of CsPb(Br_{1-x}Cl_x)₃ Perovskite: First-Principles Study with PBE–GGA and mBJ–GGA Methods

Hamid M. Ghaithan ^{1,*}, Zeyad. A. Alahmed ^{1,*}, Saif M. H. Qaid ¹ and Abdullah S. Aldwayyan ^{1,2,3,*}

¹ Physics and Astronomy Department, College of Science, King Saud University, P.O. Box 2455, Riyadh 11451, Saudi Arabia; sqaid@ksu.edu.sa

² King Abdullah Institute for Nanotechnology, King Saud University, P.O. Box 2454, Riyadh 11451, Saudi Arabia

³ K.A.CARE Energy Research and Innovation Center at Riyadh, P.O. Box 2022, Riyadh 11454, Saudi Arabia

* Correspondence: hghaithan@ksu.edu.sa (H.M.G.); zalahmed@ksu.edu.sa (Z.A.A.); dwayyan@ksu.edu.sa (A.S.A.); Tel.: +96-65-3225-7491 (H.M.G.)

Received: 14 October 2020; Accepted: 29 October 2020; Published: 3 November 2020



Abstract: The effect of halide composition on the structural, electronic, and optical properties of CsPb(Br_{1-x}Cl_x)₃ perovskite was investigated in this study. When the chloride (Cl) content of x was increased, the unit cell volume decreased with a linear function. Theoretical X-ray diffraction analyses showed that the peak (at 2θ = 30.4°) shifts to a larger angle (at 2θ = 31.9°) when the average fraction of the incorporated Cl increased. The energy bandgap (E_g) was observed to increase with the increase in Cl concentration. For x = 0.00, 0.25, 0.33, 0.50, 0.66, 0.75, and 1.00, the E_g values calculated using the Perdew–Burke–Ernzerhof potential were between 1.53 and 1.93 eV, while those calculated using the modified Becke–Johnson generalized gradient approximation (mBJ–GGA) potential were between 2.23 and 2.90 eV. The E_g calculated using the mBJ–GGA method best matched the experimental values reported. The effective masses decreased with a concentration increase of Cl to 0.33 and then increased with a further increase in the concentration of Cl. Calculated photoabsorption coefficients show a blue shift of absorption at higher Cl content. The calculations indicate that CsPb(Br_{1-x}Cl_x)₃ perovskite could be used in optical and optoelectronic devices by partly replacing bromide with chloride.

Keywords: CsPb(Br_{1-x}Cl_x)₃ perovskite; PBE–GGA and mBJ–GGA; structural properties; electronic properties; optical properties

1. Introduction

Over the last decade, organic and inorganic perovskites have gained considerable attention in the field of optoelectronics, and more recently in solar cells [1–8] and light-emitting devices [9–13], thanks to the reduced costs [14], high quantum efficiency of photoluminescence [15], and extensively tunable emission wavelengths of these materials [16–18]. Recently, inorganic mixed-halide CsPb(Br_{1-x}Cl_x)₃ compositions were used for creating various nanophotonic components because they exhibit electroluminescence in the green [12,19] to blue [20] optical ranges. CsPbBr₃ exhibits orthorhombic symmetry at temperatures below 88 °C. When the temperature increases, structural distortion occurs and the structure of CsPbBr₃ is converted to tetragonal (88 °C < T < 130 °C), and subsequently to cubic at higher temperatures (T > 130 °C) [17,18,21–38]. In comparison, at temperatures below 42 °C, CsPbCl₃ exhibits orthorhombic symmetry. When temperature increases, structural distortion occurs and the CsPbCl₃ structure is converted to tetragonal (42 °C < T < 47 °C), and subsequently to cubic at higher temperatures (T > 47 °C) [18,39]. The energy band gap (E_g) can be adjusted by adding

appropriate materials to the perovskite, which can be designed using theoretical simulations based on density functional theory (DFT) [40]. Recent studies on $\text{CsPb}(\text{Br}_{1-x}\text{Cl}_x)_3$ perovskite thin films, fabricated by sequential deposition technique, revealed an orthorhombic lattice in the case of $x = 0.1$ and 0.2 , whereas for $x = 0.4$ and 0.6 , a cubic phase was observed [41]. The electronic structure of $\text{CsPb}(\text{Br}_{1-x}\text{Cl}_x)_3$ perovskites was studied theoretically and experimentally by Tatiana G. Liashenko et al. [18]. Cl ions, which are the substitute for Br ions in the perovskite crystal lattice at room temperature, do not change its orthorhombic symmetry [18]. Generally, theoretical investigations of electronic and optical properties of organic-inorganic perovskites are often performed by first-principles calculations with the local density approximation (LDA) [42] and Perdew–Burke–Ernzerhof generalized gradient approximation (PBE–GGA) [43,44] using DFT because of their relatively cheap computational cost and reasonable accuracy [45]. The LDA and PBE–GGA potentials failed to calculate the accurate E_g and optical properties because the obtained E_g values were much smaller than the experiment values [43,44,46–48] and other possible errors [45]. In addition, the theoretical lattice parameters calculated using PBE–GGA overestimated the experimental lattice constants [45]. LDA potential usually underestimated the lattice constants, which resulted in the underestimation of E_g [45]. To overcome these significant problems of LDA and PBE–GGA potentials, the most accurate potential modified Becke–Johnson GGA (mBJ–GGA) potential was used, which is much more accurate than all other semi-local potentials for strongly correlated systems [49,50]. mBJ–GGA potential can be used for the calculation of E_g with excellent agreement with experimental values thanks to its additional dependence on kinetic energy density [49,50].

In this study, the effects of substituting Cl with Br on the structural, electronic, and optical properties of mixed Br–Cl supercell $1 \times 1 \times 4$ $\text{CsPb}(\text{Br}_{1-x}\text{Cl}_x)_3$ ($x = 0.00, 0.25, 0.33, 0.50, 0.66, 0.75$, and 1.00) are investigated using PBE–GGA and mBJ–GGA potentials. The calculated values were compared to the previous experimental [51–56] and theoretical [27,33,57–68] results to verify the validity of the DFT calculation. The effect of spin-orbital coupling (SOC) [57–60] was included in the calculation because of the heavy lead (Pb) element. By increasing the Cl content x from 0.00 to 1.00 , the lattice constants and E_g were calculated. In addition, for these mixed-halide perovskites, the effective masses of charge carriers, the binding energy of the exciton, the absorption coefficients, the optical conductivity, the dielectric constants, and the reflectivity were calculated in detail.

2. Computational Method

The full-potential linearized augmented plane wave method [61,62] based on DFT [63], as implemented in the WIEN2k code [64], has been used in the calculation. The structural properties for $\text{CsPb}(\text{Br}_{1-x}\text{Cl}_x)_3$ ($x = 0.00, 0.25, 0.33, 0.50, 0.66, 0.75$, and 1.00) were performed using Wu and Cohen (GGA–WC) potential [65]. For the electronic and optical properties, mBJ–GGA [66] and PBE–GGA potentials were used [67]. The mBJ–GGA potential with the SOC effect was included in our DFT calculation because of the heavy Pb element.

The $R_{\text{MT}}^* k_{\text{max}}$ value was set at 9.0 (R_{MT} is the smallest muffin-tin radius in the unit cell and k_{max} is the maximum value of the reciprocal lattice vectors). The R_{MT} values were set at 2.5 a.u for (Cs, Pb, and Br) and 2.41 a.u for Cl in such a way that the muffin-tin spheres do not overlap. To ensure the accuracy of our calculations, we considered $G_{\text{max}} = 12$ and $l_{\text{max}} = 10$. The irreducible Brillouin zone (IBZ) was produced using 500 k-points ($12 \times 12 \times 3$ mesh grids) and the self-consistent convergence of total energy was set at 10^{-4} Ry.

3. Results

3.1. Structural Properties

CsPbBr_3 and CsPbCl_3 have cubic structures with space group $\text{Pm}\bar{3}\text{m}$ (no. 221); the unit cell contains one formula unit. To simulate $\text{CsPb}(\text{Br}_{1-x}\text{Cl}_x)_3$, a tetragonal $1 \times 1 \times 4$ supercell with 20 atoms was used. For $x = 0.00, 0.25, 0.33, 0.50, 0.66, 0.75$, and 1.00 , a supercell with 0, 3, 4, 6, 8, 9, and 12

atoms of bromide was substituted with chloride atoms, respectively. See the Supplementary Materials, Tables S1–S7, for more details.

Figure 1 shows the crystal structure of $1 \times 1 \times 4$ supercell $\text{CsPb}(\text{Br}_{1-x}\text{Cl}_x)_3$ formed by cubic CsPbBr_3 and CsPbCl_3 .

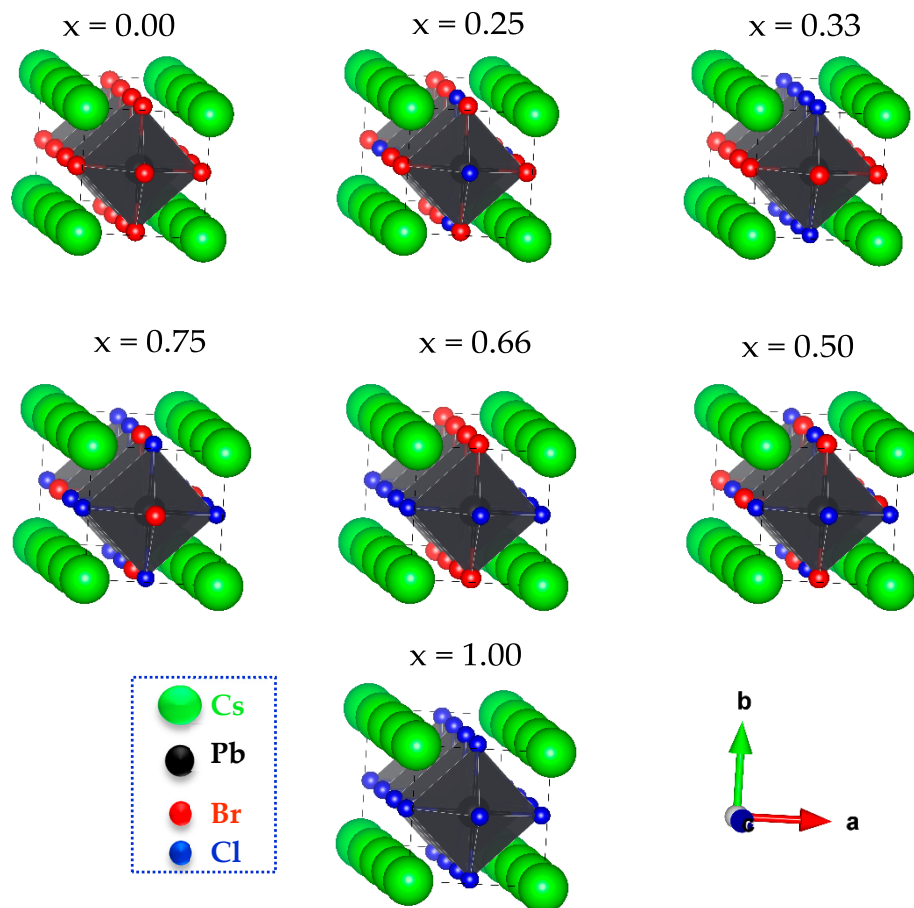


Figure 1. Atomic structures of $\text{CsPb}(\text{Br}_{1-x}\text{Cl}_x)_3$, with $x = 0.00, 0.25, 0.33, 0.50, 0.66, 0.75,$ and 1.00 for different Cl content (x).

The WC–GGA potential was determined by evaluating the ground state properties. These properties include the lattice constant a , bulk modulus B , and its pressure derivative B' . Structural optimization was performed by minimizing total energy with respect to cell volume, and the results of total energy versus unit-cell volume were fitted with Murnaghan’s state-of-the-art equation [68]. The total energy versus volume graph is shown in Figure 2. The results of a , B , and B' are shown in Table 1 with the corresponding theoretical and experimental data available in the literature. As shown in Table 1, the lattice constants of the CsPbBr_3 and CsPbCl_3 structures are in good agreement with recent theoretical and experimental results, thereby proving that our computational parameters are valid.

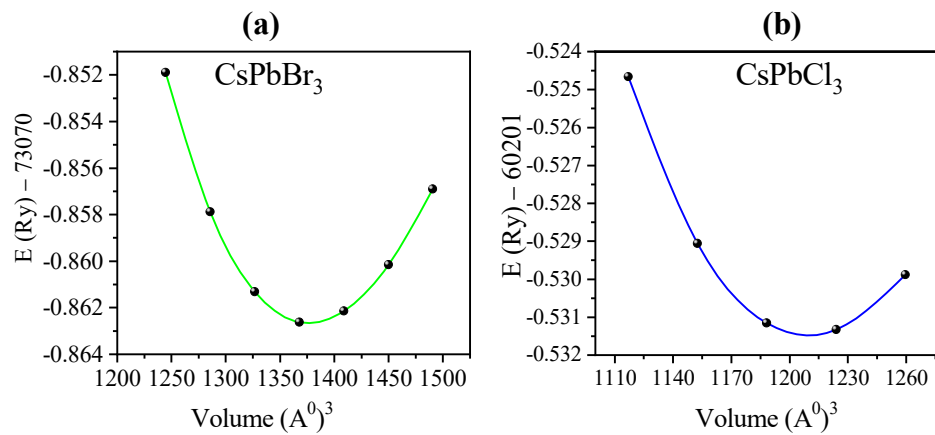


Figure 2. Calculated total energy versus volume of (a) CsPbBr₃ and (b) CsPbCl₃ via (Wu and Cohen generalized gradient approximation (WC-GGA)) potential.

Moreover, excellent agreement was observed between our obtained value of the lattice parameter for CsPbBr₃ (5.8859 Å) and its experimental value of 5.85 (Å) obtained in [69]. Moreover, the value of the lattice parameter for CsPbCl₃ was 5.6379 Å, which was in excellent agreement with the experimental value of 5.605 Å obtained in [70]. Theoretical X-ray diffraction (XRD) patterns were obtained using the visualization for electronic and structural analysis (VESTA 3, Ibaraki, Japan) [71] (see Figure 3). The diffraction peaks of CsPbBr₃ moved toward CsPbCl₃ when x changed from 0.00 to 1.00. As shown in Table 1, when the Cl content x increases from 0.00 to 1.00, the volume of the unit-cell decreases in proportion x with the function of $V(x) = 815.29916 - 112.58513x$ (Å)³, as shown in Figure 4.

Table 1. Calculated structural parameters; lattice constants a, b, and c (Å); unit cell volume V (Å)³; bulk modulus B (GPa); and its derivative B' of CsPb(Br_{1-x}Cl_x)₃ perovskite by Wu and Cohen generalized gradient approximation (WC-GGA) potential. mBJ, modified Becke–Johnson; LDA, local density approximation; PBE, Perdew–Burke–Ernzerhof.

CsPb(Br _{1-x} Cl _x) ₃	Present Work				Other Calculations (Exp.)		
	a (Å)	V (Å) ³	B (GPa)	B'	a (Å)	B (GPa)	B'
CsPbBr ₃	a = 5.874	810.703	20.7379	4.881	5.84 (WC-GGA) [72]	23.5 [72]	5.0 [72]
					5.86 (TB-mBJ) * [73]		
CsPbBr _{2.75} Cl _{0.25}	a = 5.801 c = 5.855	807.008			5.74 (LDA) [74,75]		
					6.005 (PBE-GGA) [23]		
CsPbBr ₂ Cl	a = 5.784 c = 5.748	774.139			5.87 (PBEsol) [23]		
					5.87 (PBE-GGA) [76]		
CsPbBr _{1.5} Cl _{1.5}	a = 5.739 c = 5.7395	756.278			5.77 (LDA) [23]		
					6.0039 (PBE-GGA) [77]		
CsPbBrCl ₂	a = 5.695 c = 5.6947	738.692			(5.874) [36]		
					(5.85) [69]		
CsPbBr _{0.25} Cl _{2.75}	a = 5.672 c = 5.6722	730.005			a = 6.005		
					c = 5.859 (PBE-GGA) [78]		
CsPbBr _{0.25} Cl _{2.75}	a = 5.672 c = 5.6722	730.005			a = 5.708		
					c = 6.012 (PBE-GGA) [78]		
CsPbBr _{0.25} Cl _{2.75}	a = 5.672 c = 5.6722	730.005			a = 5.718		
					c = 5.874 (PBE-GGA) [78]		
CsPbBr _{0.25} Cl _{2.75}	a = 5.672 c = 5.6722	730.005			a = 5.725		
					c = 6.012 (PBE-GGA) [78]		
CsPbBr _{0.25} Cl _{2.75}	a = 5.672 c = 5.6722	730.005			a = 5.728		
					c = 5.879 (PBE-GGA) [78]		

Table 1. Cont.

					5.56 (WC-GGA) [72]		
					5.61 (TB-mBJ) [73]		
					5.73 (PBE-GGA) [79]		
					5.49 (LDA) [75]		
					5.743 (PBE-GGA) [80]	25.8 [72]	
					5.726 (PBE-GGA) [78]	22.59 [81]	5.0 [72]
					5.728 (PBE-GGA) [81]	25.447 [82]	4.33 [81]
					5.618 (PBE-GGA) [82]	26.33 [73]	4.4 [82]
					5.740 (LDA) [74]		
					5.603 (PBE-GGA) [55]		
					5.605 [70,83]		
					5.61 [55]		
					5.6228 [30]		

* Tran and Blaha modified Becke-Johnson potential.

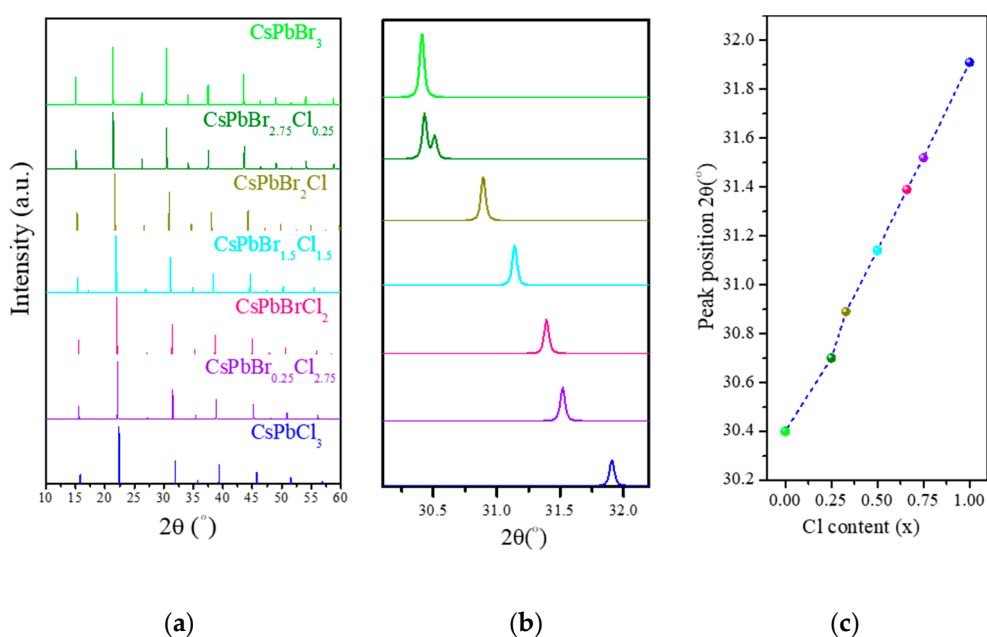


Figure 3. (a) Theoretical X-ray diffraction (XRD) patterns of CsPb(Br_{1-x}Cl_x)₃ obtained using visualization for electronic and structural analysis (VESTA) software, (b) XRD patterns ($2\theta = 30^\circ\text{--}32.1^\circ$), and (c) the peak position versus Cl content (x).

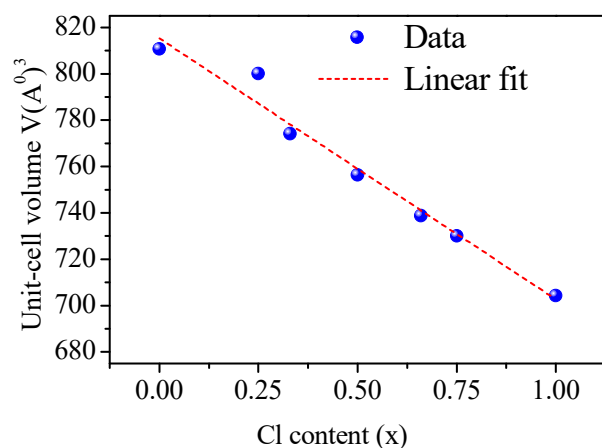


Figure 4. Unit-cell volume versus Cl content (x).

3.2. Electronic Properties

3.2.1. Electronic Band Structure

First, the electronic structures for $\text{CsPb}(\text{Br}_{1-x}\text{Cl}_x)_3$ were calculated by PBE–GGA and mBJ–GGA potentials without/with SOC. Figure 5 shows the calculated band structures of $\text{CsPb}(\text{Br}_{1-x}\text{Cl}_x)_3$ using the mBJ–GGA potentials without/with SOC. In contrast, Figure 6 shows those using the potential of PBE–GGA without SOC. The band structures have a direct transition character at M, which can improve the photoabsorption coefficient and accelerate the rate of radiative recombination [84]. The calculated E_g for CsPbBr_3 , $\text{CsPbBr}_{2.75}\text{Cl}_{0.25}$, CsPbBr_2Cl , $\text{CsPbBr}_{1.5}\text{Cl}_{1.5}$, CsPbBrCl_2 , $\text{CsPbBr}_{0.25}\text{Cl}_{2.75}$, and CsPbCl_3 based on the mBJ–GGA potential are 2.23, 2.46, 2.40, 2.51, 2.59, 2.64, and 2.90 eV, respectively, whereas the E_g values obtained using the PBE–GGA potential are 1.53, 1.68, 1.56, 1.69, 1.71, 1.77, and 1.93 eV, respectively, as shown in Table 2. The E_g calculated using mBJ–GGA were the closest to the experimental values [51–55].

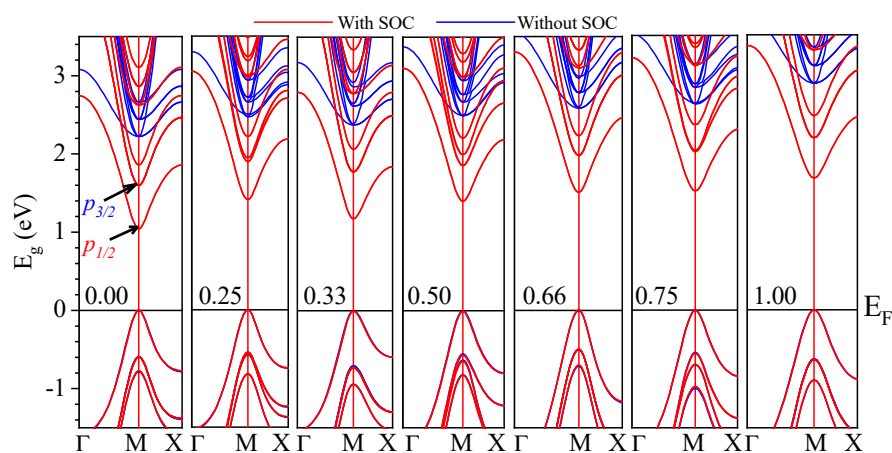


Figure 5. Calculated band structures of $\text{CsPb}(\text{Br}_{1-x}\text{Cl}_x)_3$ using the modified Becke–Johnson (mBJ)-GGA potential without/with spin-orbital coupling (SOC).

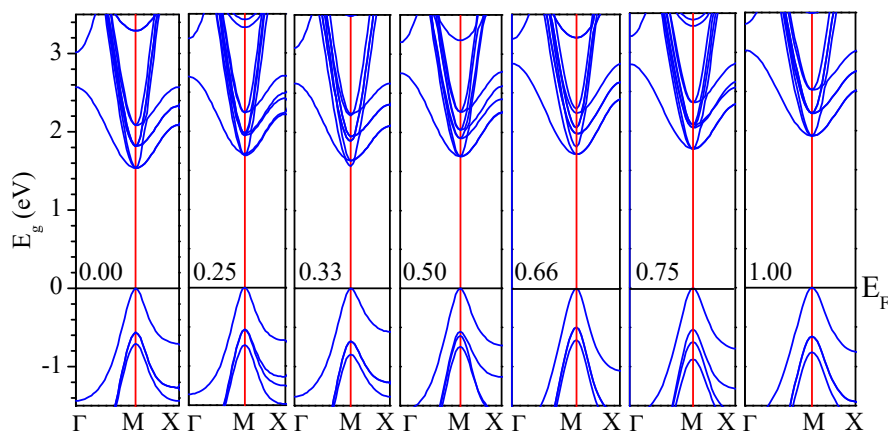


Figure 6. Calculated band structures of $\text{CsPb}(\text{Br}_{1-x}\text{Cl}_x)_3$ using the Perdew–Burke–Ernzerhof (PBE)-GGA potential.

By including the effect of SOC, the calculated E_g values are smaller than the experimental by approximately 1.23 and 1.28 eV for pure CsPbBr_3 and CsPbCl_3 , respectively, and result in more reasonable band dispersions [85,86]. The SOC causes the conduction band (CB) to decrease by splitting it into a twofold degenerated state ($p_{1/2}$) corresponding to light electrons and a fourfold degenerate state ($p_{3/2}$) corresponding to heavy electrons at this point [57,87,88]. In contrast, the valance band (VB)

showed no significant change in this area [57,87,88]. The correction was thus applied to the E_g with the following equation [78,84,89]:

$$\Delta E_g(A_{1-x}B_x) = (1-x)\Delta E_g(A) + x\Delta E_g(B) \quad (1)$$

where $\Delta E_g(A_{1-x}B_x)$, $\Delta E_g(A)$, and $\Delta E_g(B)$ are the E_g corrections for the $\text{CsPb}(\text{Br}_{1-x}\text{Cl}_x)_3$, CsPbBr_3 , and CsPbCl_3 compounds, respectively. Figure 7 shows the calculated E_g using PBE-GGA, mBJ-GGA, mBJ-GGA + SOC, and corrected mBJ-GGA + SOC(C). The calculated E_g by mBJ-GGA and mBJ-GGA + SOC(C) are in good agreement with the experimental values [53,55]. The small differences between the theoretical and experimental values are mainly attributed to the changed size for different mixed-halide [84], as depicted in the XRD patterns and the small $1 \times 1 \times 4$ supercell models.

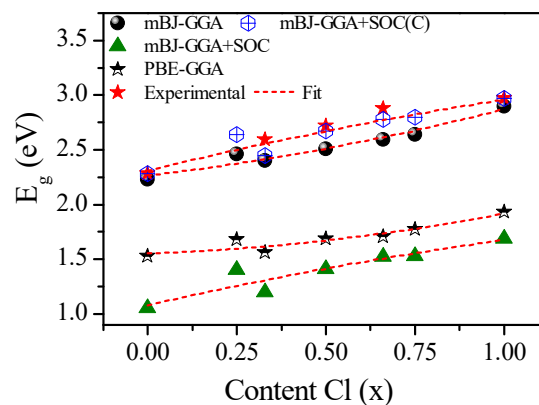


Figure 7. Band gaps of $\text{CsPb}(\text{Br}_{1-x}\text{Cl}_x)_3$ using the PBE-GGA and mBJ-GGA potentials with/without SOC. By applying the band gap correction, we get the mixed ratio band gaps of inorganic mixed halide perovskite compared with the experimental results.

The optical bowing parameter (b) was calculated for determining the relationship between the E_g and the Cl composition x [78,90,91] using the following equation:

$$\Delta E_g(x) = bx(x-1) = E_g(x) - [(1-x)E_g(A) + xE_g(B)] \quad (2)$$

where b is the bowing parameter; $E_g(A)$ and $E_g(B)$ are the band gaps of pure A and B, respectively; and $E_g(x)$ is the bandgap of A, B mixed-halide perovskites with the composition x . The dependence of the obtained E_g on the concentration of Cl (x) was given by fitting the nonlinear variation with the quadratic function as follows:

$$E_g^{(\text{PBE-GGA})}(x) = 1.55235 + 0.11317x + 0.25154x^2 \quad (3)$$

$$E_g^{(\text{mBJ-GGA})}(x) = 2.26601 + 0.37552x + 0.23037x^2 \quad (4)$$

$$E_g^{(\text{mBJ-GGA})}_{\text{SOC}}(x) = 1.08065 + 0.73866x - 0.14156x^2 \quad (5)$$

$$E_g^{(\text{mBJ-GGA})}_{\text{SOC(C)}}(x) = 2.31016 + 0.79639x - 0.14902x^2 \quad (6)$$

Table 2. Calculated E_g (eV) values of $\text{CsPb}(\text{Br}_{1-x}\text{Cl}_x)_3$ perovskite using PBE-GGA, mBJ-GGA, and mBJ-GGA + spin-orbital coupling (SOC) potentials, and mBJ-GGA + SOC(C).

$\text{CsPb}(\text{Br}_{1-x}\text{Cl}_x)_3$	E_g (eV)				Other (Exp.)
	This Work				
	PBE-GGA	mBJ-GGA	mBJ-GGA + SOC	mBJ-GGA + SOC (C)	
CsPbBr_3	1.53	2.23	1.05	2.28	2.34 (GW) [74] 1.61 (PBE-GGA) [23] 2.36 (nTmBj) [23] 2.228 (KTB-mBj) * [92] 2.08 (GLLB-SC) ** [93] 2.10 (QE) *** [35] 2.50 (mBJ-GGA) [77] (2.36) [51,94] (2.32) [52] (2.282) [53] (2.35) [95]
$\text{CsPbBr}_{2.75}\text{Cl}_{0.25}$	1.68	2.46	1.40	2.64	1.809 (PBE-GGA) [78]
CsPbBr_2Cl	1.56	2.40	1.20	2.45	1.827 (PBE-GGA) [78] (2.59) [94]
$\text{CsPbBr}_{1.5}\text{Cl}_{1.5}$	1.69	2.51	1.41	2.67	1.859 (PBE-GGA) [78] (2.72) [94]
CsPbBrCl_2	1.71	2.59	1.52	2.78	1.881 (PBE-GGA) [78] (2.88) [94]
$\text{CsPbBr}_{0.25}\text{Cl}_{2.75}$	1.77	2.64	1.53	2.80	2.05 (PBE-GGA) [78]
CsPbCl_3	1.93	2.90	1.69	2.97	2.20 (PBE-GGA) [78,96] 2.829 (KTB-mBj) [92] 2.92 (HSE) **** [79] 3.406 (PBE-GGA) [82] 2.88 (GW) [74] 2.74 (TB-mBj) [73] 2.168 (PBE-GGA) [23] 3.10 (nTmBj) [23] (3.00) [54] (2.97) [55] (3.04) [95](2.98) [94]

* Koller, Tran, and Blaha modified Becke-Johnson potential; ** Gritsenko, van Leeuwen, van Lenthe, and Baerends-Solid and Correlation; *** Quantum Espresso 6.0; **** Hybrid nonlocal exchange-correlation functional.

These results indicate the bowing parameters $b = 0.25154, 0.23037, -0.14156,$ and -0.14902 eV for the E_g obtained using PBE-GGA, mBJ-GGA, mBJ-GGA + SOC, and mBJ-GGA + SOC(C), respectively.

The influences of the dispersive nature of the conduction band (CB) and valence band (VB) on the effective masses (m_e^* and m_h^*) are shown in Figure 8. The effective masses are related to carrier mobility, which is an essential criterion for the excellent power efficiency of photovoltaic materials [85]. m_e^* and m_h^* at the band edges are related to the band dispersions. As a result, the effective masses at the CB minimum (CBM) and VB maximum (VBM) were approximated by a parabola [85,97–99]. By fitting the VB and CB edges, the effective mass (m^*) was evaluated numerically using the following equations:

$$(m^*)_{ij} = \hbar^2 \left[\frac{\partial^2 \varepsilon_n(\vec{k})}{\partial k_i \partial k_j} \right]^{-1} \quad i, j = x, y, z \quad (7)$$

where m^* is the effective mass of the charge carrier, i and j are the reciprocal components, $\varepsilon_n(\vec{k})$ is the energy dispersion function of the n^{th} band, \vec{k} represents the wave vector, and \hbar represents the reduced Planck constant.

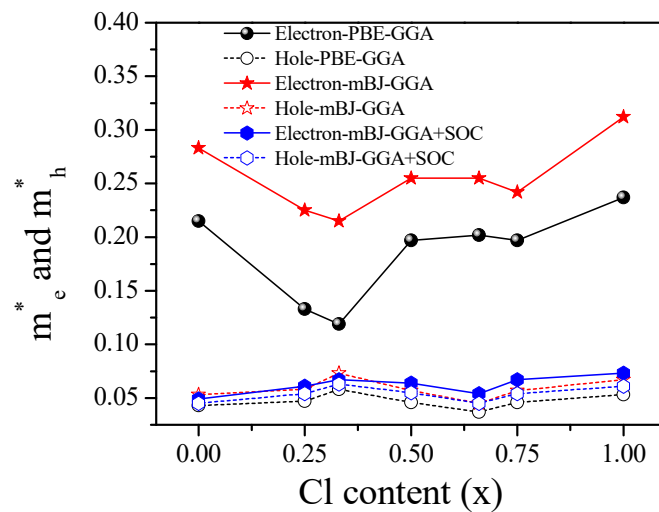


Figure 8. Effect of Cl concentration on the electron and hole effective masses for CsPb(Br_{1-x}Cl_x)₃ perovskites.

The mBJ-GGA calculation without SOC results in an accurate E_g value; however, the previous studies stated that the introduction of SOC increases band dispersion and results in more accurate effective masses with respect to DFT calculation without SOC [23,78,79,86,92,96,100–102]. Therefore, we employ mBJ-GGA + SOC to evaluate the effective charge masses. The values of m_e^* and m_h^* decreased significantly with the increase in Cl concentration up to 0.33 owing to the decrease of parabolic nature of the band structure [103]. The increased parabolic nature caused a drastic increase of the effective mass of carriers for high concentration of Cl [103]. The calculated effective charge masses around the M point of the Brillouin zone obtained by evaluating the second derivatives are shown in Table S8 (Supplementary Materials). The reduced masses μ_r were calculated using the following equation:

$$\mu_r = \frac{m_e^* m_h^*}{m_e^* + m_h^*} \quad (8)$$

The effective Bohr diameter of a Wannier-Mott exciton (a_0) can be defined [99] using the following equation:

$$a_0 = \frac{2\hbar^2 \varepsilon(\infty)}{\mu_r e^2} \quad (9)$$

where $\varepsilon(\infty)$ is the dielectric constant in the limit of infinite wavelength, and the exciton binding energy (E_b) is given by the following:

$$E_b = \frac{2\hbar^2 \varepsilon(\infty)}{\mu_r a_0^2} \quad (10)$$

For calculating E_b , we need to know the dielectric constant of the material $\varepsilon(\infty)$ and the reduced masses (μ_r), which can be obtained by DFT calculation. The estimated a_0 and E_b values were between 5.6 and 8.9 nm and between 41 and 72 meV, respectively, which were in good agreement with other theoretical [16,75,100,104,105] and experimental [106,107] values. A weaker E_b indicates that the charge carriers behave more like free charge carriers [99].

The dependence of the obtained a_0 and E_b values on the concentration of Cl (x) was determined by fitting the nonlinear variation as Cl concentration x with the linear and quadratic functions as follows:

$$a_0^{\text{PBE-GGA}}(x) = 13.6268 - 4.12266 x \quad (11)$$

$$a_0^{\text{mBJ-GGA}}(x) = 8.16334 - 1.5024 x \quad (12)$$

$$E_b^{\text{(PBE-GGA)}}(x) = 22.29863 - 0.92682 x + 17.41855 x^2 \quad (13)$$

$$E_b^{(\text{mBJ-GGA})}(x) = 44.29984 - 24.98693 x + 49.22733 x^2 \quad (14)$$

These results indicate the Bohr diameter bowing parameters of $b = -4.12266$ and -1.5024 nm obtained using PBE-GGA and mBJ-GGA, respectively. These results show that a_0 decreased with the increase in Cl concentration, as shown in Figure 9a. Furthermore, the bowing parameters $b = 17.41855$ and 49.22733 meV of E_b using PBE-GGA and mBJ-GGA indicated the decrease in E_b with the increase in Cl concentration (x), as shown in Figure 9b.

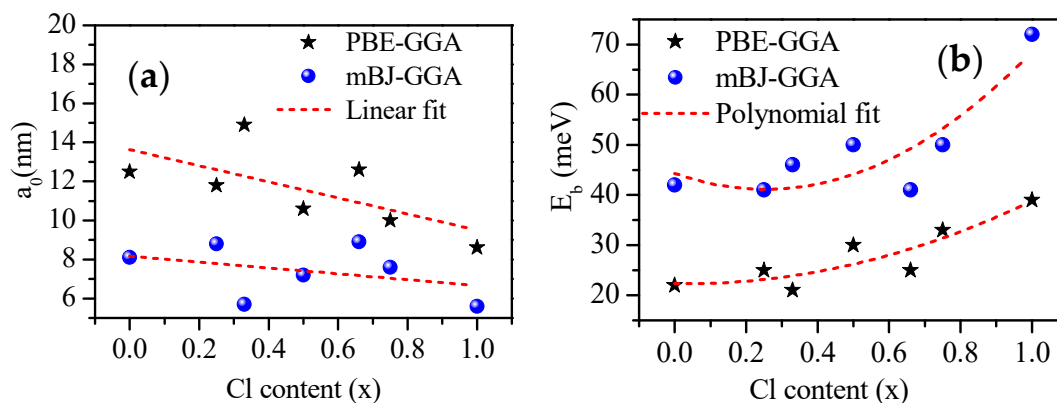


Figure 9. (a) Bohr diameter a_0 (nm) and (b) exciton binding energy E_b (meV) with respect to Cl content (x).

3.2.2. Density of States (DOS)

The total DOS (TDOS) was calculated using the mBJ-GGA potential, as shown in Figure 10. However, as the concentration (x) increased from 0.00 to 1.00, the DOS edges changed. The partial DOS (PDOS) shown in Figure 11 are based on the mBJ-GGA potential, because we are interested in the valence band (VB) and conduction band (CB) components. Previous studies have shown that inorganic cation Cs^+ does not contribute to VB maximum (VBM) and CB minimum (CBM), and only maintains overall load neutrality and structural stability [23,26,37,72,75,78,79,82,85,92,93,100,101,108,109]. Therefore, we observed only the states of Pb and halogen elements (Cl and Br), as shown in Figure 11. The VBM originates mainly from the p orbitals of Br and Cl, and a small number of contributions from s orbitals of Pb can also be observed. The CBM originated from the p states of Pb and halogen elements (Cl and Br). The CB structure is relatively similar for all of the compounds, and the CBM for each compound comprises mainly p orbitals of Pb and halogen elements (Cl and Br). The uppermost VB is steep, while the lowermost CB in PDOS is relatively flat.

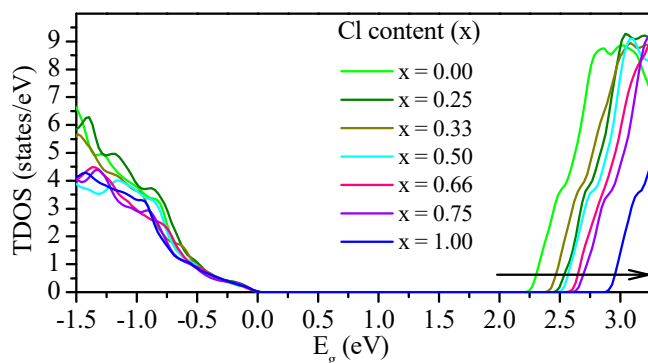


Figure 10. Total density of states (TDOS) of $\text{CsPb}(\text{Br}_{1-x}\text{Cl}_x)_3$ calculated using the mBJ-GGA potential.

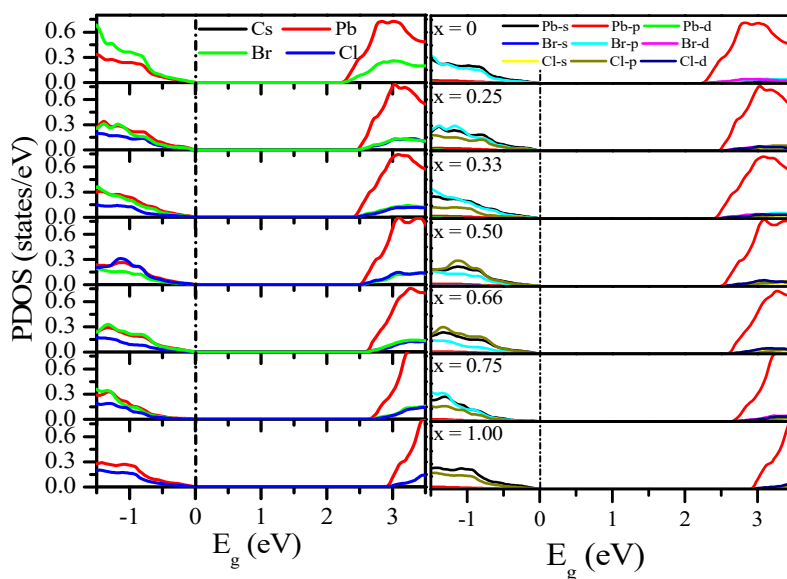


Figure 11. Calculated partial DOS (PDOS) of $\text{CsPb}(\text{Br}_{1-x}\text{Cl}_x)_3$ calculated using the mBJ–GGA potential without SOC.

For a detailed view of the band structure of $\text{CsPbBr}_{1.5}\text{Cl}_{1.5}$, PDOS was plotted on the band structure using the mBJ–GGA potential (Figure 12a). The PDOS (Figure 12b) indicated that the effects of the Cs atoms did not follow any specific rules, whereas it shows that the E_g trends are the result of the effects of Pb and Br [93]. Similar band structures of CsPbBr_3 and CsPbCl_3 with PDOS are shown in Figure S1 (Supplementary Materials).

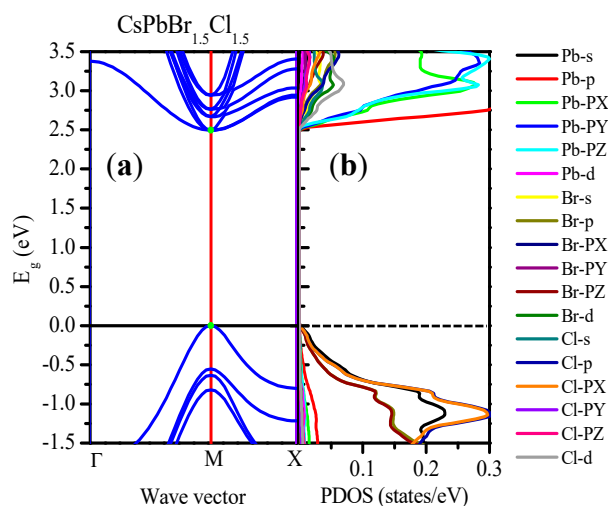


Figure 12. (a) Band structures and (b) PDOS of $\text{CsPbBr}_{1.5}\text{Cl}_{1.5}$ obtained using the mBJ–GGA potential.

To support this observation, the total charge density distributions are calculated and presented in the (001) plane, as shown in Figure 13a–g, with the structures adjacent to each concentration. The nature of bonding among the atoms could be analyzed using the map of electronic charge density distribution [72,109]. According to the Pauling scale, the electro-negativity of Cs, Pb, Br, and Cl is 0.79, 2.33, 2.96, and 3.16, respectively. For the description of the bonding character, the difference of the electro-negativity ($X_A - X_B$) is crucial [110], where X_A and X_B are the electro-negativities of the A and

B atoms, respectively. The percentage of the ionic character (IC) of the bonding can be obtained from the following equation [111]:

$$\% \text{ IC} = \left[1 - e^{-(0.25)(\chi_A - \chi_B)^2} \right] * 100 \quad (15)$$

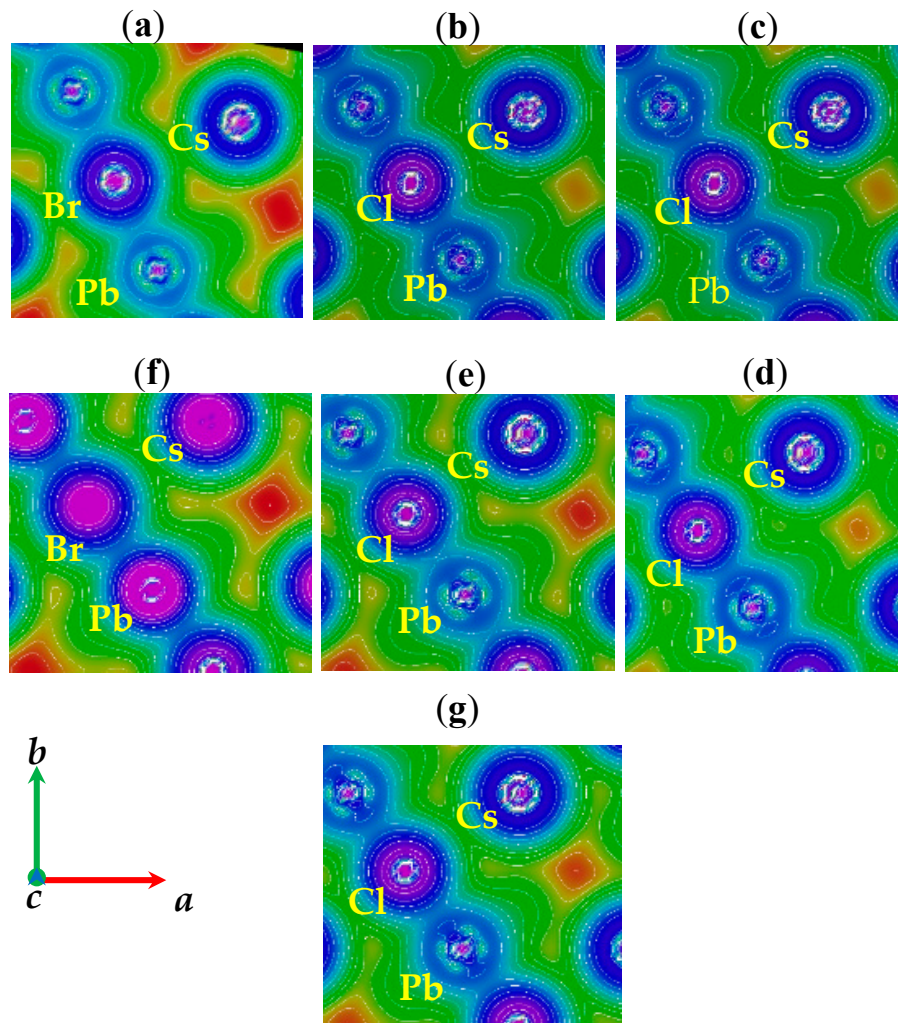


Figure 13. Calculated electron density in the (001) plane of $\text{CsPb}(\text{Br}_{1-x}\text{Cl}_x)_3$. (a) $x = 0.00$, (b) $x = 0.25$, (c) $x = 0.33$, (d) $x = 0.50$, (e) $x = 0.66$, (f) $x = 0.75$, and (g) $x = 1.00$ using the mBJ–GGA potential.

Using this equation, the obtained % IC of Cs–Br, Cs–Cl, Pb–Br, and Pb–Cl was 69.85, 75.44, 10.02, and 15.82, which indicated that the bond between Cs–Cl/Br is mostly ionic and partially covalent. In contrast, the Pb–Cl/Br bond is mostly covalent and partially ionic. Strong covalent bonds between Pb–halides have also been predicted by previous reports [72,79,110,112].

3.3. Optical Properties

The study of the optical properties of the $\text{CsPb}(\text{Br}_{1-x}\text{Cl}_x)_3$ perovskite is essential because of its potential for use in photonic and optoelectronic applications. Calculations of dielectric functions with both real $\epsilon_1(\omega)$ and imaginary $\epsilon_2(\omega)$ parts, refractive index $n(\omega)$, extinction coefficient $k(\omega)$, absorption coefficient $\alpha(\omega)$, optical conductivity $\sigma(\omega)$, and reflectivity $R(\omega)$ were explored by mBJ–GGA potential. These optical parameters can be attracted by the knowledge of the complex dielectric

function $\varepsilon(\omega) = \varepsilon_1(\omega) + i\varepsilon_2(\omega)$. The imaginary part of the dielectric function $\varepsilon_2(\omega)$, according to the perturbation theory, is given by the following equation [113,114]:

$$\varepsilon_2(\omega) = \left(\frac{\hbar^2 e^2}{\pi \omega^2 m^2} \right) \sum_{ij} \int d^3k \langle i_k | p^\alpha | j_k \rangle \langle j_k | p^\beta | i_k \rangle \times \delta(\varepsilon_{i_k} - \varepsilon_{j_k} - \omega) \quad (16)$$

where p is the moment matrix element between the band α and β states within the crystal momentum k . i_k and j_k are the crystal wave functions corresponding to the conduction and valence bands with the crystal wave vector k , respectively. The real part $\varepsilon_1(\omega)$ of the dielectric function can be expressed as follows [114]:

$$\varepsilon_1(\omega) = 1 + \frac{2}{\pi} p \int_0^\infty \frac{\omega' \varepsilon_2(\omega')}{(\omega')^2 - (\omega)^2} d\omega \quad (17)$$

where p is the value of the principal of the integral.

The absorption coefficient, optical conductivity, refractive index, extinction coefficient, and reflectance denoted by $\alpha(\omega)$, $\sigma(\omega)$, $n(\omega)$, $k(\omega)$, and $R(\omega)$, respectively, are directly related to the $\varepsilon_1(\omega)$ and $\varepsilon_2(\omega)$ [113–116].

The calculated $\varepsilon_1(\omega)$ and $\varepsilon_2(\omega)$ are shown in Figure 14a,b. As shown in Figure 14a, the static dielectric constant $\varepsilon_1(0)$ is given by the low energy limit of $\varepsilon_1(\omega)$. The peaks of $\varepsilon_1(\omega)$ shifted to higher energy as x increased from 0.00 to 1.00. The results obtained using mBJ–GGA for $\varepsilon_1(0)$ at various Cl concentrations (x) are presented in Table 3 and shown in Figure 17. $\varepsilon_1(0)$ decreased with an increase in the concentration of Cl, consistent with an increase in E_g . The results obey the following equation:

$$\varepsilon_1(x) = 3.77052 - 0.4113x - 0.09431x^2 \quad (18)$$

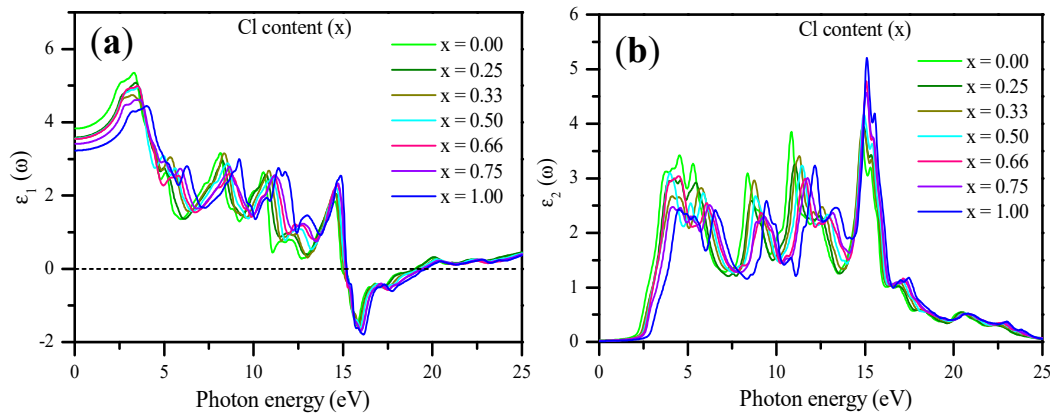


Figure 14. Calculated (a) real dielectric function $\varepsilon_1(\omega)$ and (b) imaginary dielectric function $\varepsilon_2(\omega)$ of $\text{CsPb}(\text{Br}_{1-x}\text{Cl}_x)_3$ with respect to Cl content (x) using the mBJ–GGA potential.

Table 3. Calculation of static optical parameters $\epsilon_1(0)$, refractive index $n(0)$, and reflectivity $R(0)$ for $\text{CsPb}(\text{Br}_{1-x}\text{Cl}_x)_3$ compounds.

$\text{CsPb}(\text{Br}_{1-x}\text{Cl}_x)_3$	mBJ–GGA (others)		
	$\epsilon_1(0)$	$n(0)$	$R(0)\%$
CsPbBr_3	3.82	1.96	
	(4.30) [104]	Exp. (1.85–2.3)	10.50
	(4.60) [23]	[56]	(13.4) [72]
	(4.63) [72]	(2.152) [72]	
$\text{CsPbBr}_{2.75}\text{Cl}_{0.25}$	3.59	1.897	9.65
CsPbBr_2Cl	3.57	1.890	9.55
$\text{CsPbBr}_{1.5}\text{Cl}_{1.5}$	3.56	1.882	9.52
CsPbBrCl_2	3.55	1.880	9.36
$\text{CsPbBr}_{0.25}\text{Cl}_{2.75}$	3.41	1.848	8.85
CsPbCl_3	3.23		
	(3.69) [104]	1.798	8.11
	(3.00) [81]	(1.739) [81]	(12.7) [72]
	(4.10) [23]	(2.105) [72]	(10) [82]
	(4.43) [72]		

For CsPbBr_3 , $\epsilon_1(0)$ was 3.82, which agrees well with the result obtained in the previous studies [23,72,105]. Figure 14b shows the behavior of $\epsilon_2(\omega)$ for all Cl concentrations. For $x = 0.00, 0.25, 0.33, 0.50, 0.66, 0.75$, and 1.00 , the critical points in $\epsilon_2(\omega)$ occurred at approximately 2.14, 2.25, 2.28, 2.34, 2.45, 2.55, and 2.84 eV, respectively, which were closely related to the direct E_g values of 2.26, 2.47, 2.39, 2.51, 2.58, 2.64, and 2.90 eV, respectively.

The refractive index $n(\omega)$ and extinction coefficients $k(\omega)$ were calculated using the mBJ–GGA potential, as shown in Figure 15a,b. The spectrum of $n(\omega)$ closely resembles the spectrum of $\epsilon_1(\omega)$ [117]. For CsPbBr_3 , the calculated $n(0)$ value was 1.96, which agrees well with the previous theoretical and experimental values [56,72]. For CsPbCl_3 , $n(0)$ was 1.798, which agrees well with the previous value [72,81]. The calculated $n(0)$ versus the Cl concentration (x) is expressed as follows:

$$n(x) = 1.94752 - 0.13036x - 0.00939x^2 \quad (19)$$

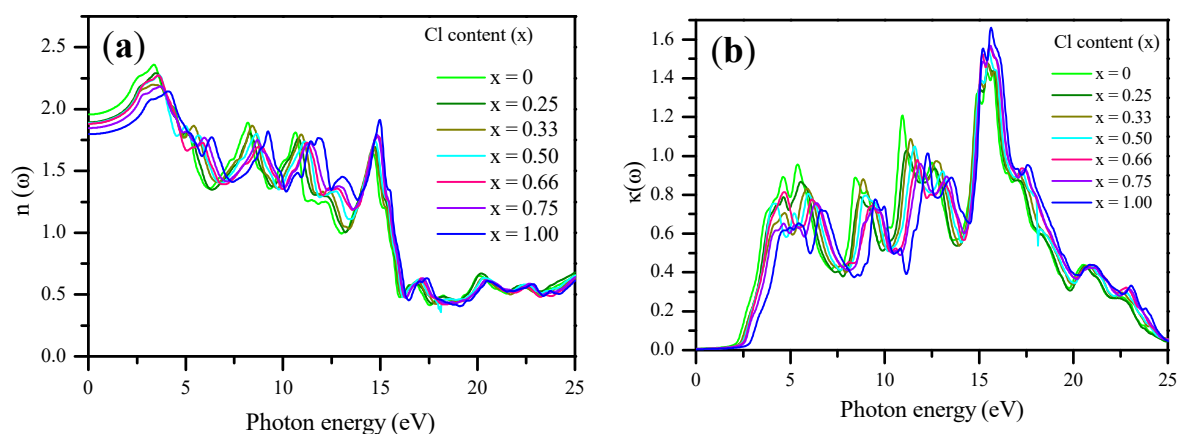
**Figure 15.** Calculated (a) refraction indices $n(\omega)$ and (b) extinction coefficients $k(\omega)$ of $\text{CsPb}(\text{Br}_{1-x}\text{Cl}_x)_3$ with respect to Cl content (x) using the mBJ–GGA potential.

Figure 15b shows that $k(\omega)$ depends on the concentration of Cl similar to that of $\epsilon_2(\omega)$. The peak value of $k(\omega)$ shifted to lower energies as Cl concentration increased from 0.00 to 1.00.

The initial reflectivity $R(\omega)$ values were around 10.50% and 8.11% at zero frequency, which then increased to 18.62% (at 3.53 eV) and 15.24% (at 4.30 eV) for CsPbBr_3 ($x = 0.00$) and CsPbCl_3 ($x = 1.00$),

respectively, as shown in Figure 16. The maximum reflectivity peaks of 48%, 46.7%, 47.8%, 48.5%, 48.7%, 48.6%, and 51% occurred at energy values of 15.88, 15.97, 16.00, 16.10, 16.16, 16.18, and 16.29 eV, respectively, and then began to fluctuate and decrease at higher energies. The value of $R(0)$ decreased with the increase in Cl concentration (x), as shown in Figure 17 and presented in Table 3. The calculated $R(0)$ versus Cl concentration (x) was fitted as follows:

$$R(x)\% = 10.3264 - 1.55348 x - 0.54961 x^2. \quad (20)$$

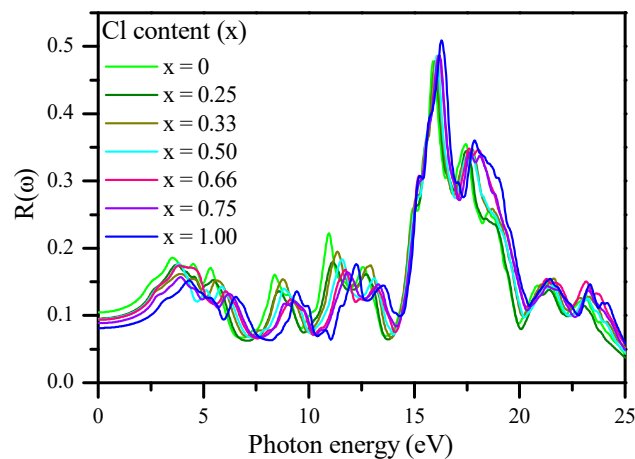


Figure 16. Calculated reflectivity spectra $R(\omega)$ of $\text{CsPb}(\text{Br}_{1-x}\text{Cl}_x)_3$ using the mBJ-GGA potential.

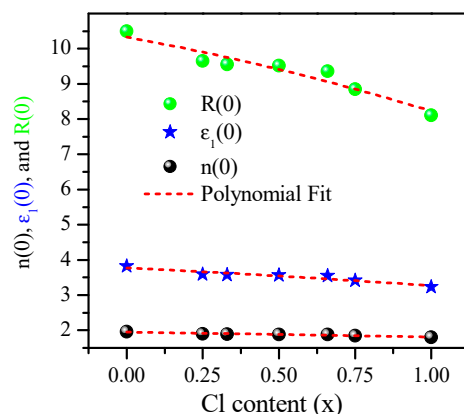


Figure 17. Static refractive index, real dielectric function, and reflectivity at zero frequency versus Cl content (x).

Figure 18a shows the absorption coefficient $\alpha(\omega)$. With the increase in Cl concentration (x), the absorption edge shifted to higher energy. The wide absorption range from visible to ultraviolet indicates that these compounds are useful for various optical and optoelectronic applications [72]. Figure 18b shows similar features of the optical conductivity $\sigma(\omega)$ characteristics, and provides information on the effects of external parameters on the electronic structure [118].

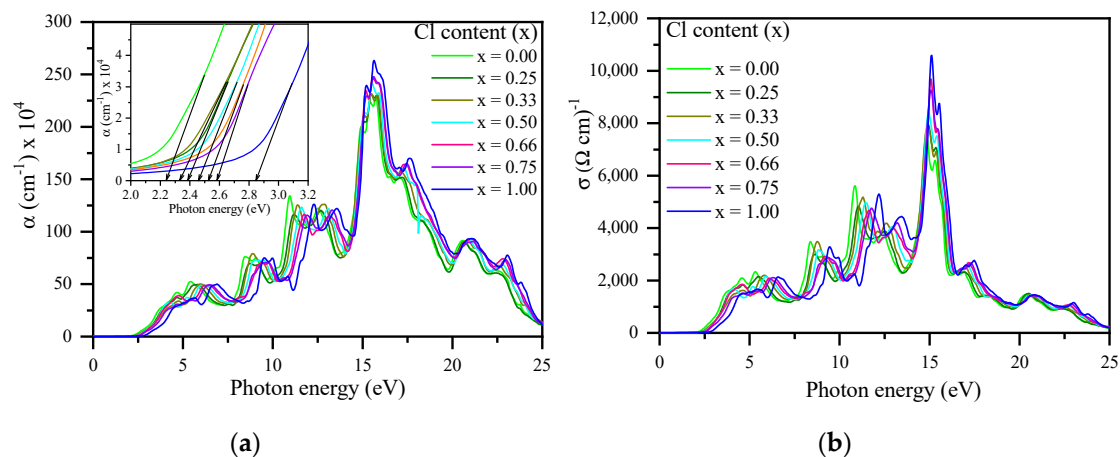


Figure 18. (a) Calculated absorption spectra $\alpha(\omega)$ and (b) conductivity $\sigma(\omega)$ of CsPb(Br_{1-x}Cl_x)₃ with respect to Cl content (x) using the mBJ-GGA potential. Inset: absorption spectra in the range from 2.0 to 3.2 eV.

4. Conclusions

In this study, we investigated the influence of halide composition on the structural, electronic, and optical properties of the mixed-halide perovskites CsPb(Br_{1-x}Cl_x)₃ using DFT. When the Cl content x was increased from 0.00 to 1.00, a decrease in unit-cell volume was observed. Theoretical XRD analyses revealed that the peak shifts to larger angles when the concentration of Cl increases. An increase in E_g was observed with an increase in the concentration of Cl. The E_g values calculated using the PBE-GGA potential were between 1.53 and 1.93 eV, while those calculated using the mBJ-GGA potential were between 2.23 and 2.90 eV. The increase in E_g with the increase in Cl content was due to the fact that the hybridization of Cl 3p states with Pb-s states was stronger than that with Br 4p states, which leads to a downshift of VBM and a decrease in the lattice constant. The calculated E_g and exciton binding energy E_b using mBJ-GGA potential best matched the previously reported experimental and theoretical values. The effective masses of electron and hole (m_e^* and m_h^*) are correlated with the energies of E_g . The calculated photoabsorption coefficients display a blue shift of the absorption at a higher Cl concentration.

Supplementary Materials: The following are available online at <http://www.mdpi.com/1996-1944/13/21/4944/s1>, Tables S1–S7: Structural properties of CsPb(Br_{1-x}Cl_x)₃ Perovskite, Table S8: Effective mass of electron (m_e^*) and hole (m_h^*), reduced mass (μ_r), bohr diameter (a_0), dielectric constant (ϵ), and exciton binding energy (E_b) values calculated by PBE-GGA, mBJ-GGA, and mBJ-GGA + SOC potentials, Figure S1: Band structures and PDOS of (a) CsPbBr₃ and (b) CsPbCl₃ obtained using the mBJ-GGA potential.

Author Contributions: Conceptualization, H.M.G. and Z.A.A.; methodology, H.M.G. and Z.A.A.; software, H.M.G. and Z.A.A.; validation, Z.A.A. and A.S.A.; formal analysis, H.M.G. and Z.A.A.; investigation, H.M.G., Z.A.A., and A.S.A.; writing—original draft preparation, H.M.G.; writing—review and editing, H.M.G., Z.A.A., A.S.A., and S.M.H.Q.; supervision, A.S.A. and Z.A.A.; funding acquisition, A.S.A. All authors have read and agreed to the published version of the manuscript.

Funding: This research received no external funding.

Acknowledgments: The authors extend their appreciation to the Deputyship for Research & Innovation, “Ministry of Education” in Saudi Arabia for funding this research work through the project number IFKSURG-265.

Conflicts of Interest: The authors declare no conflict of interest.

References

- Haddad, J.; Krogmeier, B.; Klingebiel, B.; Krückemeier, L.; Melhem, S.; Liu, Z.; Hüpkens, J.; Mathur, S.; Kirchartz, T. Analyzing Interface Recombination in Lead-Halide Perovskite Solar Cells with Organic and Inorganic Hole-Transport Layers. *Adv. Mater. Interfaces* **2020**, *7*, 2000366. [[CrossRef](#)]

2. Zhao, Y.; Duan, J.; Wang, Y.; Yang, X.; Tang, Q. Precise stress control of inorganic perovskite films for carbon-based solar cells with an ultrahigh voltage of 1.622 V. *Nano Energy* **2020**, *67*, 104286. [[CrossRef](#)]
3. Duan, J.; Wei, J.; Tang, Q.; Li, Q. Unveiling the interfacial charge extraction kinetics in inorganic perovskite solar cells with formamidinium lead halide (FAPbX₃) nanocrystals. *Sol. Energy* **2020**, *195*, 644–650. [[CrossRef](#)]
4. Ouedraogo, N.A.N.; Chen, Y.; Xiao, Y.Y.; Meng, Q.; Han, C.B.; Yan, H.; Zhang, Y. Stability of all-inorganic perovskite solar cells. *Nano Energy* **2020**, *67*, 104249. [[CrossRef](#)]
5. Feng, J.; Zhu, X.; Yang, Z.; Zhang, X.; Niu, J.; Wang, Z.; Zuo, S.; Priya, S.; Liu, S. (Frank); Yang, D. Record Efficiency Stable Flexible Perovskite Solar Cell Using Effective Additive Assistant Strategy. *Adv. Mater.* **2018**, *30*, e1801418. [[CrossRef](#)]
6. Wang, K.; Jin, Z.; Liang, L.; Bian, H.; Bai, D.; Wang, H.; Zhang, J.; Wang, Q.; Shengzhong, L. All-inorganic cesium lead iodide perovskite solar cells with stabilized efficiency beyond 15%. *Nat. Commun.* **2018**, *9*, 1–8. [[CrossRef](#)]
7. Kim, H.S.; Lee, C.R.; Im, J.H.; Lee, K.B.; Moehl, T.; Marchioro, A.; Moon, S.J.; Humphry-Baker, R.; Yum, J.H.; Moser, J.E.; et al. Lead iodide perovskite sensitized all-solid-state submicron thin film mesoscopic solar cell with efficiency exceeding 9%. *Sci. Rep.* **2012**, *2*, 591. [[CrossRef](#)]
8. Eperon, G.E.; Paternò, G.M.; Sutton, R.J.; Zampetti, A.; Haghighirad, A.A.; Cacialli, F.; Snaith, H.J. Inorganic caesium lead iodide perovskite solar cells. *J. Mater. Chem. A* **2015**, *3*, 19688–19695. [[CrossRef](#)]
9. Lin, K.; Xing, J.; Quan, L.N.; de Arquer, F.P.G.; Gong, X.; Lu, J.; Xie, L.; Zhao, W.; Zhang, D.; Yan, C.; et al. Perovskite light-emitting diodes with external quantum efficiency exceeding 20 per cent. *Nature* **2018**, *562*, 245–248. [[CrossRef](#)]
10. Matsushima, T.; Bencheikh, F.; Komino, T.; Leyden, M.R.; Sandanayaka, A.S.D.; Qin, C.; Adachi, C. High performance from extraordinarily thick organic light-emitting diodes. *Nature* **2019**, *572*, 502–506. [[CrossRef](#)]
11. Zhang, Q.; Tavakoli, M.M.; Gu, L.; Zhang, D.; Tang, L.; Gao, Y.; Guo, J.; Lin, Y.; Leung, S.F.; Poddar, S.; et al. Efficient metal halide perovskite light-emitting diodes with significantly improved light extraction on nanophotonic substrates. *Nat. Commun.* **2019**, *10*, 727. [[CrossRef](#)]
12. Veldhuis, S.A.; Boix, P.P.; Yantara, N.; Li, M.; Sum, T.C.; Mathews, N.; Mhaisalkar, S.G. Perovskite Materials for Light-Emitting Diodes and Lasers. *Adv. Mater.* **2016**, *28*, 6804–6834. [[CrossRef](#)] [[PubMed](#)]
13. Tan, Z.K.; Moghaddam, R.S.; Lai, M.L.; Docampo, P.; Higler, R.; Deschler, F.; Price, M.; Sadhanala, A.; Pazos, L.M.; Credgington, D.; et al. Bright light-emitting diodes based on organometal halide perovskite. *Nat. Nanotechnol.* **2014**, *9*, 687–692. [[CrossRef](#)] [[PubMed](#)]
14. Even, J.; Pedesseau, L.; Jancu, J.M.; Katan, C. DFT and $k \cdot p$ modelling of the phase transitions of lead and tin halide perovskites for photovoltaic cells. *Phys. Status Solidi Rapid Res. Lett.* **2014**, *8*, 31–35. [[CrossRef](#)]
15. Droseros, N.; Longo, G.; Brauer, J.C.; Sessolo, M.; Bolink, H.J.; Banerji, N. Origin of the Enhanced Photoluminescence Quantum Yield in MAPbBr₃ Perovskite with Reduced Crystal Size. *ACS Energy Lett.* **2018**, *3*, 1458–1466. [[CrossRef](#)]
16. Protesescu, L.; Yakunin, S.; Bodnarchuk, M.I.; Krieg, F.; Caputo, R.; Hendon, C.H.; Yang, R.X.; Walsh, A.; Kovalenko, M.V. Nanocrystals of Cesium Lead Halide Perovskites (CsPbX₃, X = Cl, Br, and I): Novel Optoelectronic Materials Showing Bright Emission with Wide Color Gamut. *Nano Lett.* **2015**, *15*, 3692–3696. [[CrossRef](#)]
17. Nedelcu, G.; Protesescu, L.; Yakunin, S.; Bodnarchuk, M.I.; Grotevent, M.J.; Kovalenko, M.V. Fast Anion-Exchange in Highly Luminescent Nanocrystals of Cesium Lead Halide Perovskites (CsPbX₃, X = Cl, Br, I). *Nano Lett.* **2015**, *15*, 5635–5640. [[CrossRef](#)]
18. Liashenko, T.G.; Cherotchenko, E.D.; Pushkarev, A.P.; Pakštas, V.; Naujokaitis, A.; Khubezhov, S.A.; Polozkov, R.G.; Agapev, K.B.; Zakhidov, A.A.; Shelykh, I.A.; et al. Electronic structure of CsPbBr_{3-x}Cl_x perovskites: Synthesis, experimental characterization, and DFT simulations. *Phys. Chem. Chem. Phys.* **2019**, *21*, 18930–18938. [[CrossRef](#)]
19. Zhang, L.; Yang, X.; Jiang, Q.; Wang, P.; Yin, Z.; Zhang, X.; Tan, H.; Yang, Y.M.; Wei, M.; Sutherland, B.R.; et al. Ultra-bright and highly efficient inorganic based perovskite light-emitting diodes. *Nat. Commun.* **2017**, *8*, 15640. [[CrossRef](#)]
20. Song, J.; Li, J.; Li, X.; Xu, L.; Dong, Y.; Zeng, H. Quantum Dot Light-Emitting Diodes Based on Inorganic Perovskite Cesium Lead Halides (CsPbX₃). *Adv. Mater.* **2015**, *27*, 7162–7167. [[CrossRef](#)]

21. Zhang, X.; Jin, Z.; Zhang, J.; Bai, D.; Bian, H.; Wang, K.; Sun, J.; Wang, Q.; Liu, S.F. All-Ambient Processed Binary CsPbBr₃-CsPb₂Br₅ Perovskites with Synergistic Enhancement for High-Efficiency Cs-Pb-Br-Based Solar Cells. *ACS Appl. Mater. Interfaces* **2018**, *10*, 7145–7154. [[CrossRef](#)]
22. Stoumpos, C.C.; Malliakas, C.D.; Peters, J.A.; Liu, Z.; Sebastian, M.; Im, J.; Chasapis, T.C.; Wibowo, A.C.; Chung, D.Y.; Freeman, A.J.; et al. Crystal growth of the perovskite semiconductor CsPbBr₃: A new material for high-energy radiation detection. *Cryst. Growth Des.* **2013**, *13*, 2722–2727. [[CrossRef](#)]
23. Ahmad, M.; Rehman, G.; Ali, L.; Shafiq, M.; Iqbal, R.; Ahmad, R.; Khan, T.; Jalali-Asadabadi, S.; Maqbool, M.; Ahmad, I. Structural, electronic and optical properties of CsPbX₃ (X=Cl, Br, I) for energy storage and hybrid solar cell applications. *J. Alloys Compd.* **2017**, *705*, 828–839. [[CrossRef](#)]
24. Yaffe, O.; Guo, Y.; Hull, T.; Stoumpos, C.C.; Tan, L.Z.; Egger, D.A.; Zheng, F.; Szapak, G.; Semonin, O.E.; Beecher, A.N.; et al. The nature of dynamic disorder in lead halide perovskite crystals (Conference Presentation). *Phys. Chem. Interfaces Nanomater. XV* **2016**. [[CrossRef](#)]
25. Rodova, M.; Brozek, J.; Knizek, K.; Nitsch, K. Phase transitions in ternary caesium lead bromide. *J. Therm. Anal. Calorim.* **2003**, *71*, 667–673. [[CrossRef](#)]
26. Bechtel, J.S.; Van Der Ven, A. First-principles thermodynamics study of phase stability in inorganic halide perovskite solid solutions. *Phys. Rev. Mater.* **2018**, *2*, 045401. [[CrossRef](#)]
27. Zhang, M.; Zheng, Z.; Fu, Q.; Chen, Z.; He, J.; Zhang, S.; Yan, L.; Hu, Y.; Luo, W. Growth and characterization of all-inorganic lead halide perovskite semiconductor CsPbBr₃ single crystals. *CrystEngComm* **2017**, *19*, 6797–6803. [[CrossRef](#)]
28. He, Y.; Matei, L.; Jung, H.J.; McCall, K.M.; Chen, M.; Stoumpos, C.C.; Liu, Z.; Peters, J.A.; Chung, D.Y.; Wessels, B.W.; et al. High spectral resolution of gamma-rays at room temperature by perovskite CsPbBr₃ single crystals. *Nat. Commun.* **2018**, *9*, 1–8. [[CrossRef](#)]
29. Qiao, B.; Song, P.; Cao, J.; Zhao, S.; Shen, Z.; Di, G.; Liang, Z.; Xu, Z.; Song, D.; Xu, X. Water-resistant, monodispersed and stably luminescent CsPbBr₃/CsPb₂Br₅ core-shell-like structure lead halide perovskite nanocrystals. *Nanotechnology* **2017**, *28*, 445602. [[CrossRef](#)]
30. Bertolotti, F.; Protesescu, L.; Kovalenko, M.V.; Yakunin, S.; Cervellino, A.; Billinge, S.J.L.; Terban, M.W.; Pedersen, J.S.; Masciocchi, N.; Guagliardi, A. Coherent Nanotwins and Dynamic Disorder in Cesium Lead Halide Perovskite Nanocrystals. *ACS Nano* **2017**, *11*, 3819–3831. [[CrossRef](#)]
31. Dos Reis, R.; Yang, H.; Ophus, C.; Ercius, P.; Bizzari, G.; Perrodin, D.; Shalapska, T.; Bourret, E.; Ciston, J.; Dahmen, U. Determination of the structural phase and octahedral rotation angle in halide perovskites. *Appl. Phys. Lett.* **2018**, *112*, 071901. [[CrossRef](#)]
32. Cottingham, P.; Brutchey, R.L. On the crystal structure of colloiddally prepared CsPbBr₃ quantum dots. *Chem. Commun.* **2016**, *52*, 5246–5249. [[CrossRef](#)]
33. Wolf, C.; Lee, T.W. Exciton and lattice dynamics in low-temperature processable CsPbBr₃ thin-films. *Mater. Today Energy* **2018**, *7*, 199–207. [[CrossRef](#)]
34. Zhang, M.; Zheng, Z.; Fu, Q.; Chen, Z.; He, J.; Zhang, S.; Chen, C.; Luo, W. Synthesis and single crystal growth of perovskite semiconductor CsPbBr₃. *J. Cryst. Growth* **2018**, *484*, 37–42. [[CrossRef](#)]
35. Goesten, M.G.; Hoffmann, R. Mirrors of Bonding in Metal Halide Perovskites. *J. Am. Chem. Soc.* **2018**, *140*, 12996–13010. [[CrossRef](#)]
36. Møller, C.K. The Structure of Perovskite-Like Cæsium Plumbo Trihalides. *Mater. Fys. Medd. Dan. Vid. Selsk* **1959**, *32*, 1–27.
37. Yang, R.X.; Skelton, J.M.; Da Silva, E.L.; Frost, J.M.; Walsh, A. Spontaneous octahedral tilting in the cubic inorganic cesium halide perovskites CsSnX₃ and CsPbX₃ (X = F, Cl, Br, I). *J. Phys. Chem. Lett.* **2017**, *8*, 4720–4726. [[CrossRef](#)] [[PubMed](#)]
38. Kirschner, M.S.; Diroll, B.T.; Guo, P.; Harvey, S.M.; Helweh, W.; Flanders, N.C.; Brumberg, A.; Watkins, N.E.; Leonard, A.A.; Evans, A.M.; et al. Photoinduced, reversible phase transitions in all-inorganic perovskite nanocrystals. *Nat. Commun.* **2019**, *10*, 1–8. [[CrossRef](#)]
39. Plesko, S.; Kind, R.; Roos, J. Structural Phase Transitions in CsPbCl₃ and RbCdCl₃. *J. Phys. Soc. Jpn.* **1978**, *45*, 553–557. [[CrossRef](#)]
40. Yu, H.S.; Li, S.L.; Truhlar, D.G. Perspective: Kohn-Sham density functional theory descending a staircase. *J. Chem. Phys.* **2016**, *145*, 130901. [[CrossRef](#)]

41. Li, B.; Zhang, Y.; Zhang, L.; Yin, L. PbCl₂-tuned inorganic cubic CsPbBr₃(Cl) perovskite solar cells with enhanced electron lifetime, diffusion length and photovoltaic performance. *J. Power Sources* **2017**, *360*, 11–20. [[CrossRef](#)]
42. Kohn, W.; Sham, L.J. Self-Consistent Equations Including Exchange and Correlation Effects. *Phys. Rev.* **1965**, *140*, A1133. [[CrossRef](#)]
43. Perdew, J.P.; Burke, K.; Ernzerhof, M. Generalized Gradient Approximation Made Simple. *Phys. Rev. Lett.* **1996**, *66*, 3865–3868. [[CrossRef](#)]
44. Ziesche, P.; Kurth, S.; Perdew, J.P. Density functionals from LDA to GGA. *Comput. Mater. Sci.* **1998**, *11*, 122–127. [[CrossRef](#)]
45. Raju, N.P.; Thangavel, R. Theoretical investigation of spin–orbit coupling on structural, electronic and optical properties for CuAB₂ (A = Sb, Bi; B = S, Se) compounds using Tran–Blaha-modified Becke–Johnson method: A first-principles approach. *J. Alloys Compd.* **2020**, *2*, 154621. [[CrossRef](#)]
46. Tran, F.; Blaha, P. Implementation of screened hybrid functionals based on the Yukawa potential within the LAPW basis set. *Phys. Rev. B* **2011**, *83*, 235118. [[CrossRef](#)]
47. Staroverov, V.N.; Scuseria, G.E.; Tao, J.; Perdew, J.P. Tests of a ladder of density functionals for bulk solids and surfaces. *Phys. Rev. B* **2004**, *69*, 075102. [[CrossRef](#)]
48. Kurth, S.; Perdew, J.P.; Blaha, P. Molecular and solid-state tests of density functional approximations: LSD, GGAs, and Meta-GGAs. *Int. J. Quantum Chem.* **1999**, *75*, 889–909. [[CrossRef](#)]
49. Camargo-Martínez, J.A.; Baquero, R. The band gap problem: The accuracy of the wien2k code confronted. *Rev. Mex. Fis.* **2013**, *59*, 453–459.
50. Tran, F.; Blaha, P. Importance of the Kinetic Energy Density for Band Gap Calculations in Solids with Density Functional Theory. *J. Phys. Chem. A* **2017**, *121*, 3318–3325. [[CrossRef](#)]
51. Akkerman, Q.A.; Motti, S.G.; Srimath Kandada, A.R.; Mosconi, E.; D’Innocenzo, V.; Bertoni, G.; Marras, S.; Kamino, B.A.; Miranda, L.; De Angelis, F.; et al. Solution Synthesis Approach to Colloidal Cesium Lead Halide Perovskite Nanoplatelets with Monolayer-Level Thickness Control. *J. Am. Chem. Soc.* **2016**, *138*, 1010–1016. [[CrossRef](#)]
52. Li, Y.; Duan, J.; Yuan, H.; Zhao, Y.; He, B.; Tang, Q. Lattice Modulation of Alkali Metal Cations Doped Cs_{1-x}R_xPbBr₃ Halides for Inorganic Perovskite Solar Cells. *Sol. RRL* **2018**, *2*, 1800164. [[CrossRef](#)]
53. Qaid, S.M.H.; Al-Asbahi, B.A.; Ghaithan, H.M.; AlSalhi, M.S.; Al dwayyan, A.S. Optical and structural properties of CsPbBr₃ perovskite quantum dots/PFO polymer composite thin films. *J. Colloid Interface Sci.* **2020**, *563*, 426–434. [[CrossRef](#)]
54. Heidrich, K.; Schäfer, W.; Schreiber, M.; Söchtig, J.; Trendel, G.; Treusch, J.; Grandke, T.; Stolz, H.J. Electronic structure, photoemission spectra, and vacuum-ultraviolet optical spectra of CsPbCl₃ and CsPbBr₃. *Phys. Rev. B* **1981**, *24*, 5642–5649. [[CrossRef](#)]
55. Pandey, N.; Kumar, A.; Chakrabarti, S. Investigation of the structural, electronic, and optical properties of Mn-doped CsPbCl₃: Theory and experiment. *RSC Adv.* **2019**, *9*, 29556–29565. [[CrossRef](#)]
56. Yakunin, S.; Protesescu, L.; Krieg, F.; Bodnarchuk, M.I.; Nedelcu, G.; Humer, M.; De Luca, G.; Fiebig, M.; Heiss, W.; Kovalenko, M.V. Low-threshold amplified spontaneous emission and lasing from colloidal nanocrystals of caesium lead halide perovskites lead halide perovskites. *Nat. Commun.* **2015**, *6*, 8056. [[CrossRef](#)]
57. Afsari, M.; Boochani, A.; Hantezadeh, M.; Elahi, S.M. Topological nature in cubic phase of perovskite CsPbI₃: By DFT. *Solid State Commun.* **2017**, *259*, 10–15. [[CrossRef](#)]
58. Zhang, Q.; Su, R.; Du, W.; Liu, X.; Zhao, L.; Ha, S.T.; Xiong, Q. Advances in Small Perovskite-Based Lasers. *Small Methods* **2017**, *1*, 1700163. [[CrossRef](#)]
59. Even, J.; Pedesseau, L.; Jancu, J.M.; Katan, C. Importance of spin-orbit coupling in hybrid organic/inorganic perovskites for photovoltaic applications. *J. Phys. Chem. Lett.* **2013**, *4*, 2999–3005. [[CrossRef](#)]
60. Wang, K.; Yang, Q.; Duan, J.; Zhang, C.; Zhao, F.; Yu, H.; Hu, B. Spin-Polarized Electronic Transport through Ferromagnet/Organic–Inorganic Hybrid Perovskite Spinterfaces at Room Temperature. *Adv. Mater. Interfaces* **2019**, 1900718. [[CrossRef](#)]
61. Blaha, P.; Schwarz, K.; Trickey, S.B. Full-potential, linearized augmented plane wave programs for crystalline systems. *Comput. Phys. Commun* **1990**, *59*, 399–415. [[CrossRef](#)]
62. Madsen, G.K.H.; Blaha, P.; Schwarz, K.; Sjöstedt, E.; Nordström, L. Efficient linearization of the augmented plane-wave method. *Phys. Rev. B Condens. Matter Mater. Phys.* **2001**, *64*, 195134. [[CrossRef](#)]

63. Hohenberg, P.; Kohn, W. Inhomogeneous Electron Gas. *Phys. Rev.* **1964**, *136*, B864. [[CrossRef](#)]
64. Blaha, P.; Schwarz, K.; Madsen, G.K.H.; Kvasnicka, D.; Luitz, J. *WIEN2k, An Augmented Plane Wave + Local Orbitals Program for Calculating Crystal Properties*; Technische Universität Wien: Vienna, Austria, 2001; ISBN 3-9501031-1-2.
65. Wu, Z.; Cohen, R.E. More accurate generalized gradient approximation for solids. *Phys. Rev. B Condens. Matter Mater. Phys.* **2006**, *73*, 235116. [[CrossRef](#)]
66. Tran, F.; Blaha, P. Accurate band gaps of semiconductors and insulators with a semilocal exchange-correlation potential. *Phys. Rev. Lett.* **2009**, *102*, 226401. [[CrossRef](#)]
67. Städele, M.; Majewski, J.A.; Vogl, P.; Görling, A. Exact Kohn-Sham Exchange Potential in Semiconductors. *Phys. Rev. Lett.* **1997**, *79*, 2089–2092. [[CrossRef](#)]
68. G.F.S. The volume changes of five gases under high pressures. *J. Franklin Inst.* **1924**, *197*, 98. [[CrossRef](#)]
69. Beal, R.E.; Slotcavage, D.J.; Leijtens, T.; Bowring, A.R.; Belisle, R.A.; Nguyen, W.H.; Burkhard, G.F.; Hoke, E.T.; McGehee, M.D. Cesium Lead Halide Perovskites with Improved Stability for Tandem Solar Cells. *J. Phys. Chem. Lett.* **2016**, *7*, 746–751. [[CrossRef](#)] [[PubMed](#)]
70. Lim, A.R.; Jeong, S.Y. Twin structure by ^{133}Cs NMR in ferroelastic CsPbCl_3 crystal. *Solid State Commun.* **1999**, *110*, 131–136. [[CrossRef](#)]
71. Momma, K.; Izumi, F. VESTA 3 for three-dimensional visualization of crystal, volumetric and morphology data. *J. Appl. Crystallogr.* **2011**, *44*, 1272–1276. [[CrossRef](#)]
72. Murtaza, G.; Ahmad, I. First principle study of the structural and optoelectronic properties of cubic perovskites CsPbM_3 ($\text{M}=\text{Cl}, \text{Br}, \text{I}$). *Phys. B Condens. Matter* **2011**, *406*, 3222–3229. [[CrossRef](#)]
73. Mahmood, Q.; Hassan, M.; Rashid, M.; Haq, B.U.; Laref, A. The systematic study of mechanical, thermoelectric and optical properties of lead based halides by first principle approach. *Phys. B Condens. Matter* **2019**, *571*, 87–92. [[CrossRef](#)]
74. Jaroenjittichai, A.P.; Laosiritaworn, Y. Band alignment of cesium-based halide perovskites. *Ceram. Int.* **2018**, *44*, S161–S163. [[CrossRef](#)]
75. Chang, Y.H.; Park, C.H. First-Principles Study of the Structural and the Electronic Properties of the Lead-Halide-Based Inorganic-Organic Perovskites $(\text{CH}_3\text{NH}_3)\text{PbX}_3$ and CsPbX_3 ($\text{X} = \text{Cl}, \text{Br}, \text{I}$). *J. Korean Phys. Soc.* **2004**, *44*, 889–893.
76. Ghaithan, H.M.; AlAhmed, Z.A.; Lyras, A.; Qaid, S.M.H.; Aldwayyan, A.S. Computational Investigation of the Folded and Unfolded Band Structure and Structural and Optical Properties of $\text{CsPb}(\text{I}_{1-x}\text{Br}_x)_3$ Perovskites. *Crystals* **2020**, *10*, 342. [[CrossRef](#)]
77. Ghaithan, H.M.; Alahmed, Z.A.; Qaid, S.M.H.; Aldwayyan, A.S. First principle-based calculations of the optoelectronic features of $2 \times 2 \times 2$ $\text{CsPb}(\text{I}_{1-x}\text{Br}_x)_3$ perovskite. *Superlattices Microstruct.* **2020**, *140*, 106474. [[CrossRef](#)]
78. Chen, X.; Han, D.; Su, Y.; Zeng, Q.; Liu, L.; Shen, D. Structural and Electronic Properties of Inorganic Mixed Halide Perovskites. *Phys. Status Solidi Rapid Res. Lett.* **2018**, *12*, 1800193. [[CrossRef](#)]
79. Lang, L.; Yang, J.H.; Liu, H.R.; Xiang, H.J.; Gong, X.G. First-principles study on the electronic and optical properties of cubic ABX_3 halide perovskites. *Phys. Lett. A* **2014**, *378*, 290–293. [[CrossRef](#)]
80. Wanwieng, N.; Laosiritaworn, Y. Enthalpy of formation of $\text{CsSn}(\text{Cl}_x(\text{Br}, \text{I})_{1-x})_3$ and $\text{CsPb}(\text{Cl}_x(\text{Br}, \text{I})_{1-x})_3$. *Siam Phys. Congr.* **2018**, *1144*, 012137. [[CrossRef](#)]
81. Ghebouli, M.A.; Ghebouli, B.; Fatmi, M. First-principles calculations on structural, elastic, electronic, optical and thermal properties of CsPbCl_3 perovskite. *Phys. B Condens. Matter* **2011**, *406*, 1837–1843. [[CrossRef](#)]
82. Ilyas, B.M.; Elias, B.H. A theoretical study of perovskite CsXCl_3 ($\text{X}=\text{Pb}, \text{Cd}$) within first principles calculations. *Phys. B Condens. Matter* **2017**, *510*, 60–73. [[CrossRef](#)]
83. Möller, C.K. Crystal structure and photoconductivity of caesium plumbahalides. *Nature* **1958**, *182*, 1436. [[CrossRef](#)]
84. Su, Y.; Chen, X.; Ji, W.; Zeng, Q.; Ren, Z.; Su, Z.; Liu, L. Highly Controllable and Efficient Synthesis of Mixed-Halide CsPbX_3 ($\text{X} = \text{Cl}, \text{Br}, \text{I}$) Perovskite QDs toward the Tunability of Entire Visible Light. *ACS Appl. Mater. Interfaces* **2017**, *9*, 33020–33028. [[CrossRef](#)]
85. Yi, Z.; Fang, Z. Theoretical studies on the structural, electronic and optical properties of orthorhombic perovskites $\text{CH}_3\text{NH}_3\text{PbX}_3$ ($\text{X} = \text{I}, \text{Br}, \text{Cl}$). *J. Phys. Chem. Solids* **2017**, *110*, 145–151. [[CrossRef](#)]
86. Umari, P.; Mosconi, E.; De Angelis, F. Relativistic GW calculations on $\text{CH}_3\text{NH}_3\text{PbI}_3$ and $\text{CH}_3\text{NH}_3\text{SnI}_3$ Perovskites for Solar Cell Applications. *Sci. Rep.* **2014**, *4*, 4467. [[CrossRef](#)]

87. Ghaithan, H.M.; Alahmed, Z.A.; Qaid, S.M.H.; Hezam, M.; Aldwayyan, A.S. Density Functional Study of Cubic, Tetragonal, and Orthorhombic CsPbBr₃ Perovskite. *ACS Omega* **2020**, *5*, 7468–7480. [[CrossRef](#)]
88. Sun, P.P.; Li, Q.S.; Yang, L.N.; Li, Z.S. Theoretical insights into a potential lead-free hybrid perovskite: Substituting Pb²⁺ with Ge²⁺. *Nanoscale* **2016**, *8*, 1503–1512. [[CrossRef](#)]
89. Yin, W.J.; Yan, Y.; Wei, S.H. Anomalous alloy properties in mixed halide perovskites. *J. Phys. Chem. Lett.* **2014**, *5*, 3625–3631. [[CrossRef](#)]
90. Bellaiche, L.; Wei, S.H.; Zunger, A. Localization and percolation in semiconductor alloys: GaAsN vs GaAsP. *Phys. Rev. B Condens. Matter Mater. Phys.* **1996**, *54*, 17568–17576. [[CrossRef](#)]
91. Wei, S.H.; Zunger, A. Giant and composition-dependent optical bowing coefficient in GaAsN alloys. *Phys. Rev. Lett.* **1996**, *76*, 664–667. [[CrossRef](#)]
92. Jishi, R.A.; Ta, O.B.; Sharif, A.A. Modeling of lead halide perovskites for photovoltaic applications. *J. Phys. Chem. C* **2014**, *118*, 28344–28349. [[CrossRef](#)]
93. Mao, X.; Sun, L.; Wu, T.; Chu, T.; Deng, W.; Han, K. First-Principles Screening of All-Inorganic Lead-Free ABX₃ Perovskites. *J. Phys. Chem. C* **2018**, *122*, 7670–7675. [[CrossRef](#)]
94. Paul, T.; Chatterjee, B.K.; Maiti, S.; Sarkar, S.; Besra, N.; Das, B.K.; Panigrahi, K.J.; Thakur, S.; Ghorai, U.K.; Chattopadhyay, K.K. Tunable cathodoluminescence over the entire visible window from all-inorganic perovskite CsPbX₃ 1D architecture. *J. Mater. Chem. C* **2018**, *6*, 3322–3333. [[CrossRef](#)]
95. Diroll, B.T.; Zhou, H.; Schaller, R.D. Low-Temperature Absorption, Photoluminescence, and Lifetime of CsPbX₃ (X = Cl, Br, I) Nanocrystals. *Adv. Funct. Mater.* **2018**, *28*, 1800945. [[CrossRef](#)]
96. Castelli, I.E.; García-Lastra, J.M.; Thygesen, K.S.; Jacobsen, K.W. Bandgap calculations and trends of organometal halide perovskites. *APL Mater.* **2014**, *2*, 081514. [[CrossRef](#)]
97. Feng, J.; Xiao, B. Effective masses and electronic and optical properties of nontoxic MASnX₃ (X = Cl, Br, and I) perovskite structures as solar cell absorber: A theoretical study using HSE06. *J. Phys. Chem. C* **2014**, *118*, 19655–19660. [[CrossRef](#)]
98. Feng, J.; Xiao, B. Crystal Structures, Optical Properties, and Effective Mass Tensors of CH₃NH₃PbX₃ (X = I and Br) Phases Predicted from HSE06. *J. Phys. Chem. Lett.* **2014**, *5*, 1278–1282.
99. Jong, U.G.; Yu, C.J.; Ri, J.S.; Kim, N.H.; Ri, G.C. Influence of halide composition on the structural, electronic, and optical properties of mixed CH₃NH₃Pb(I_{1-x}Br_x)₃ perovskites calculated using the virtual crystal approximation method. *Phys. Rev. B* **2016**, *94*, 125139. [[CrossRef](#)]
100. Qian, J.; Xu, B.; Tian, W. A comprehensive theoretical study of halide perovskites ABX₃. *Org. Electron. Phys. Mater. Appl.* **2016**, *37*, 61–73. [[CrossRef](#)]
101. Yuan, Y.; Xu, R.; Xu, H.T.; Hong, F.; Xu, F.; Wang, L.J. Nature of the band gap of halide perovskites ABX₃ (A = CH₃NH₃, Cs; B = Sn, Pb; X = Cl, Br, I): First-principles calculations. *Chinese Phys. B* **2015**, *24*, 116302. [[CrossRef](#)]
102. Fang, Z.; Yi, Z. First principles study on mixed orthorhombic perovskite CH₃NH₃Pb(I_{1-x}Br_x)₃. *Chem. Phys. Lett.* **2017**, *687*, 19–22. [[CrossRef](#)]
103. Rahman, N.M.; Adnaan, M.; Adhikary, D.; Islam, M.; Alam, M.K. First-principles calculation of the optoelectronic properties of doped methylammonium lead halide perovskites: A DFT-based study. *Comput. Mater. Sci.* **2018**, *150*, 439–447. [[CrossRef](#)]
104. Kang, Y.; Han, S. Intrinsic Carrier Mobility of Cesium Lead Halide Perovskites. *Phys. Rev. Appl.* **2018**, *10*, 044013. [[CrossRef](#)]
105. Tomanová, K.; Čuba, V.; Brik, M.G.; Mihóková, E.; Martínez Turtos, R.; Lecoq, P.; Auffray, E.; Nikl, M. On the structure, synthesis, and characterization of ultrafast blue-emitting CsPbBr₃ nanoplatelets. *APL Mater.* **2019**, *7*, 011104. [[CrossRef](#)]
106. Wu, K.; Liang, G.; Shang, Q.; Ren, Y.; Kong, D.; Lian, T. Ultrafast interfacial electron and hole transfer from CsPbBr₃ perovskite quantum dots. *J. Am. Chem. Soc.* **2015**, *137*, 12792–12795. [[CrossRef](#)]
107. Du, W.; Zhang, S.; Shi, J.; Chen, J.; Wu, Z.; Mi, Y.; Liu, Z.; Li, Y.; Sui, X.; Wang, R.; et al. Strong Exciton-Photon Coupling and Lasing Behavior in All-Inorganic CsPbBr₃ Micro/Nanowire Fabry-Pérot Cavity. *ACS Photonics* **2018**, *5*, 2051–2059. [[CrossRef](#)]
108. Jin, H.; Im, J.; Freeman, A.J. Topological insulator phase in halide perovskite structures. *Phys. Rev. B Condens. Matter Mater. Phys.* **2012**, *86*, 121102. [[CrossRef](#)]

109. Sutton, R.J.; Filip, M.R.; Haghghirad, A.A.; Sakai, N.; Wenger, B.; Giustino, F.; Snaith, H.J. Cubic or Orthorhombic? Revealing the Crystal Structure of Metastable Black-Phase CsPbI₃ by Theory and Experiment. *ACS Energy Lett.* **2018**, *3*, 1787–1794. [[CrossRef](#)]
110. Reshak, A.H.; Alahmed, Z.A.; Bila, J. Phase transition in BaThO₃ from Pbnm to Ibmm turn the fundamental energy band gap from indirect to direct. *J. Alloys Compd.* **2019**, *771*, 607–613. [[CrossRef](#)]
111. Callister, W.D., Jr.; Rethwisch, D.G. *Fundamentals of Materials Science and Engineering*, 5th ed.; John Wiley & Sons Inc.: Hoboken, NJ, USA, 2018; ISBN 978-1-119-17550-6.
112. Pitriana, P.; Wungu, T.D.K.; Herman; Hidayat, R. The characteristics of band structures and crystal binding in all-inorganic perovskite APbBr₃ studied by the first principle calculations using the Density Functional Theory (DFT) method. *Results Phys.* **2019**, *15*, 102592. [[CrossRef](#)]
113. Ambrosch-Draxl, C.; Sofo, J.O. Linear optical properties of solids within the full-potential linearized augmented planewave method. *Comput. Phys. Commun.* **2006**, *175*, 1–14. [[CrossRef](#)]
114. Dar, S.A.; Sharma, R.; Srivastava, V.; Sakalle, U.K. Investigation on the electronic structure, optical, elastic, mechanical, thermodynamic and thermoelectric properties of wide band gap semiconductor double perovskite Ba₂InTaO₆. *RSC Adv.* **2019**, *9*, 9522–9532. [[CrossRef](#)]
115. Adachi, S. *Properties of Semiconductor Alloys: Group-IV, III-V and II-VI Semiconductors*; John Wiley & Sons: Hoboken, NJ, USA, 2009; ISBN 9780470744383.
116. Benchehima, M.; Abid, H.; Sadoun, A.; Chabane Chaouche, A. Optoelectronic properties of aluminum bismuth antimony ternary alloys for optical telecommunication applications: First principles calculation. *Comput. Mater. Sci.* **2018**, *155*, 224–234. [[CrossRef](#)]
117. Amin, B.; Ahmad, I.; Maqbool, M.; Goumri-Said, S.; Ahmad, R. Ab initio study of the bandgap engineering of Al_{1-x}Ga_xN for optoelectronic applications. *J. Appl. Phys.* **2011**, *109*, 023109. [[CrossRef](#)]
118. Kushwaha, A.K.; Laref, A.; Laref, S. First-Principles Investigation of Structural, Electronic, Optical, and Magnetic Properties of Ternary Mixed Compound CsTe_xS_{1-x}. *J. Electron. Mater.* **2019**, *48*, 3479–3489. [[CrossRef](#)]

Publisher's Note: MDPI stays neutral with regard to jurisdictional claims in published maps and institutional affiliations.



© 2020 by the authors. Licensee MDPI, Basel, Switzerland. This article is an open access article distributed under the terms and conditions of the Creative Commons Attribution (CC BY) license (<http://creativecommons.org/licenses/by/4.0/>).